Limnol. Oceanogr., 53(5, part 2), 2008, 2094–2111

Ocean metabolism observed with oxygen sensors on profiling floats in the South Pacific

Todd R. Martz and Kenneth S. Johnson
Monterey Bay Aquarium Research Institute, Moss Landing, California 95039

Stephen C. Riser
School of Oceanography, University of Washington, Seattle, Washington 98195

Abstract

We estimated rates of production and export in the South Pacific (80°W to 180°W in a zonal band between 35°S and 50°S) using 1.5 yr of oxygen measurements from profiling floats. Export production, calculated from oxygen utilization rates below the compensation depth from December to April, was 10.7 ± 2 mmol C m^{-2} d^{-1} (n = 36, 95% CI). The corresponding satellite net primary production was 46 ± 4 mmol C m^{-2} d^{-1}, yielding a regional e-ratio of 0.23 ± 0.05. Averaging oxygen utilization rates resulted in a net cancellation of most water mass changes related to advection and float migration. The composite vertical profile of remineralization rates, obtained by binning 36 rate profiles, agreed with published measurements based on oxygen utilization rates in hydrographic surveys and fits the classic form of a particulate organic carbon (POC) attenuation function. However, the disagreement between oxygen-based remineralization rates and those obtained by sediment traps suggests fundamental differences between these two methods. Using float data to constrain a one-dimensional mixed-layer model, the annual net community production at 45°S, 144°W was ~2.5 mol C m^{-2} yr^{-1}. Spatial trends in export production coinciding with the New Zealand shelf and Subtropical Front are identified.

The quantification of basin-scale magnitudes and trends in net primary production (NPP), net community production (NCP), and export production (EP) are required for a first-order estimate of biologically driven transport of carbon to depth (i.e., the strength of the 'biological pump'; Sarmiento and Gruber 2006). A great deal of work has focused on the links between depth-integrated rates of NPP (NPP = gross carbon fixation − autotrophic respiration), NCP (NCP = NPP − heterotrophic respiration), and EP (EP = vertical organic carbon flux). On the annual mesoscale the ocean is near steady-state and NCP ~ EP (Brix et al. 2006). The e-ratio, EP : NPP, is a fundamental term in the carbon budget because it determines what fraction of NPP is sequestered by the ocean interior for decades or longer. A primary metric of the validity of ocean ecosystem models is their ability to accurately depict export flux or e-ratios (Lima and Doney 2004).

Presently, estimates based on remote sensing provide near-comprehensive coverage of ocean NPP on large geographic scales (Behrenfeld and Falkowski 1997; Behrenfeld et al. 2005). Satellites constrain global ocean NPP to ~±10% (Falkowski et al. 1998) and local NPP to no better than ±35% (Hooker and McClain 2000). Export flux and remineralization rates have been measured throughout the ocean using a variety of techniques, including sediment traps, oxygen utilization rates, and ^{234}Th disequilibrium. Because measurements of NCP and EP are typically made at point locations on subannual timescales (often subdaily for NCP), episodic, seasonal, or annual decoupling of NCP from EP may result in a break from the steady-state paradigm at the sampling location (Plattner et al. 2005). Locally, NCP and EP are measured with accuracy of ±50% (Emerson et al. 1997). There is, however, no direct estimate of EP or NCP with spatial and temporal coverage complementary to satellite-based NPP.

Dunne et al. (2005) compiled 122 e-ratio observations spanning the past 30 yr and derived empirical relationships for EP : NPP as a function of both chlorophyll *a* (Chl *a*)–temperature and NPP–temperature. Limited agreement between these relationships and e-ratios obtained through biogeochemical Ocean General Circulation Models (OGCMs; Gehlen et al. 2006) underscores both the sparseness of data and the simplifications which are inherent, but necessary, in models. Presumably, inverse techniques provide the most reliable estimates of global EP, but there is not necessarily a consensus between models constrained by satellite vs. those constrained by hydrographic measurements. For example, Schlitzer (2002) showed that EP estimated through an inversion of the World Ocean Circulation Experiment (WOCE) data set only moderately agreed with EP calculated by transforming satellite NPP into EP using an empirical (temperature- and NPP-dependent) e-ratio (e.g., Laws et al. 2000). Clearly, modeling efforts will become more reliable as the density of EP : NPP measurements increases.

Because photosynthesis is restricted to the uppermost strata of the ocean, NCP has often been inferred from changes in the inventory of nutrients, carbon dioxide (CO_2) species, or oxygen levels from the surface to the base of the

Acknowledgments

We thank two anonymous reviewers for insightful comments that greatly improved the manuscript. Work at MBARI was supported by a grant from the David and Lucile Packard Foundation and by the National Science Foundation through the Biocomplexity in the Environment Program Grant ECS-0308070. Research at the University of Washington was supported by the National Oceanic and Atmospheric Administration Grant NA17RJ1232 Task 2 and by Office of Naval Research Contract ONR NOOO14-03-1-0446.

mixed layer or euphotic zone. Chemical sensor technology now allows similar estimates of NCP based either directly on a chemical budget or a model constrained by sensor data (Karl et al. 2003; DeGrandpre et al. 2004; Johnson et al. 2006). In contrast, estimates of EP from sensor data are few because, unlike NCP, EP occurs at *all* depths. Direct observations of EP (or related processes) require depth-resolved time series. Dissolved oxygen is a good candidate for such measurements because changes in oxygen are due mainly to respiration of exported particulate and dissolved organic matter beneath the compensation depth (Z_c, depth where NCP = 0). As discussed in this work, advection and water mass changes also affect dissolved oxygen and must be considered.

In the upper 200 m there are considerable differences in the annual cycles of oxygen. In the surface layer of the ocean, when photosynthetic rates exceed respiration, net production occurs. As depth increases, conditions shift from net production to net respiration at the compensation depth. As described by Najjar and Keeling (1997), the relative placement of mixed-layer depth (mld) and compensation depth results in distinct zones of oxygen cycles. The shallowest production zone is continuously ventilated and oxygen levels are mostly controlled by physics, remaining close to atmospheric equilibrium and out of phase with temperature throughout the year. The seasonally ventilated production zone develops a shallow (or subsurface) oxygen maximum (SOM) after the mixed layer shoals in the spring, seemingly due to trapped photosynthetically-produced oxygen. The seasonally ventilated consumption zone undergoes a ventilation–respiration cycle where, after winter mixing restores atmospheric equilibrium to water below the compensation depth, oxygen is continuously consumed once the mixed layer shoals above the compensation depth. Here, we focus on these three zones and overlook the fourth nonventilated consumption zone where advection plays a more significant role in the oxygen cycle.

Continuous oxygen measurements in combination with a physical-biogeochemical model would allow observation of many aspects of primary production and deep-sea respiration. Historically, patterns in the annual oxygen cycle have been studied at only a few locations with rather sparse (monthly) data (e.g., Hawaii Ocean Time Series [HOT], Bermuda Atlantic Time Series [BATS]) or by combining decades of accumulated data into a single climatology (Najjar and Keeling 1997). Oxygen measurements from platforms (DeGrandpre et al. 1998) and moorings (Emerson et al. 2002) are increasingly common. More recently, profiling floats (Körtzinger et al. 2005) and isopycnal Lagrangian floats (Lazarevich et al. 2004) have allowed direct observation of annual ventilation–respiration processes associated with deep wintertime mixing and summertime stratification.

Until recently, there was no easy way to extend these observations because oxygen sensors required considerable maintenance. However, it has been shown that in situ oxygen measurements can now be made over multiple years on profiling floats with little drift in sensor calibration (Körtzinger et al. 2005; Gruber et al. 2007; Johnson et al. 2007). As of May 2007, 100 profiling floats in the Argo Program had been equipped with oxygen sensors. These relatively long-lived autonomous sensors provide a unique opportunity to investigate the oxygen cycle on a scale in both space and time that was formerly unavailable. In this study, we examined oxygen production above and oxygen consumption below the compensation depth using data from floats in the South Pacific Ocean, deployed by the University of Washington as part of the international Argo Program. Net community production from the surface to the deepest annual mixed-layer depth was estimated using a 1-D mixed-layer model where productivity was treated as a tunable model parameter and found by least-squares optimization using O_2 data from the floats. We examined biologically driven oxygen changes below the compensation depth from the oxygen utilization rate. At these depths, we found a distinct seasonal cycle. The observed changes in oxygen below the compensation depth were due to remineralization of organic matter, exported out of the mixed layer by sinking, mixing, and active transport by zooplankton. These methods yielded robust estimates of annual net community and export production.

Methods

Profiling floats and study site—Since 2004, the University of Washington has deployed 24 profiling floats in the South Pacific from 80°W to 180°W across a zonal band located between 35°S and 50°S (Fig. 1). A Seabird SBE-43 oxygen sensor and a Seabird SBE-41 CTD (Conductivity, Temperature and Depth [salinity measurement]) sensor were installed on each float. Every 7 d, a measurement sequence begins with a descent to 2,000 m from a 1,000-m park depth. Temperature, conductivity (salinity), pressure, and oxygen levels are measured as the float ascends to the surface. In the upper 400 m, measurement frequency increases from 50-m to 10-m intervals.

The 40°S band of the Pacific is a transition region between the permanently stratified, oligotrophic South Pacific subtropical gyre and the seasonally stratified, mesotrophic South Pacific (Sarmiento et al. 2004). The floats are located in the vicinity of the Subtropical Front (STF), which is nominally located between 30°S and 40°S (Chaigneau and Pizarro 2005). The surface circulation at 40°S generally proceeds from west to east (South Pacific Current), but, as shown below, the floats followed a more irregular pattern, probably due to countercurrents at the park depth (1,000 m) and eddy activity. Traveling from north to south, the upper 500 m of this region is characterized by sharp decreases in salinity and temperature at the STF, with temperature decreasing steadily and salinity remaining relatively constant south of the transition region. The STF also marks north-to-south increases in surface nutrient and chlorophyll concentrations (Tsuchiya and Talley 1998). Limited information exists regarding the ecology of the South Pacific Ocean between the STF and the Subantarctic Front. Phytoplankton and zooplankton across the STF near New Zealand (Bradford-Grieve et al. 1999) and picoplankton in the South Pacific north of the STF (Grob et al. 2007) have been characterized, yet the

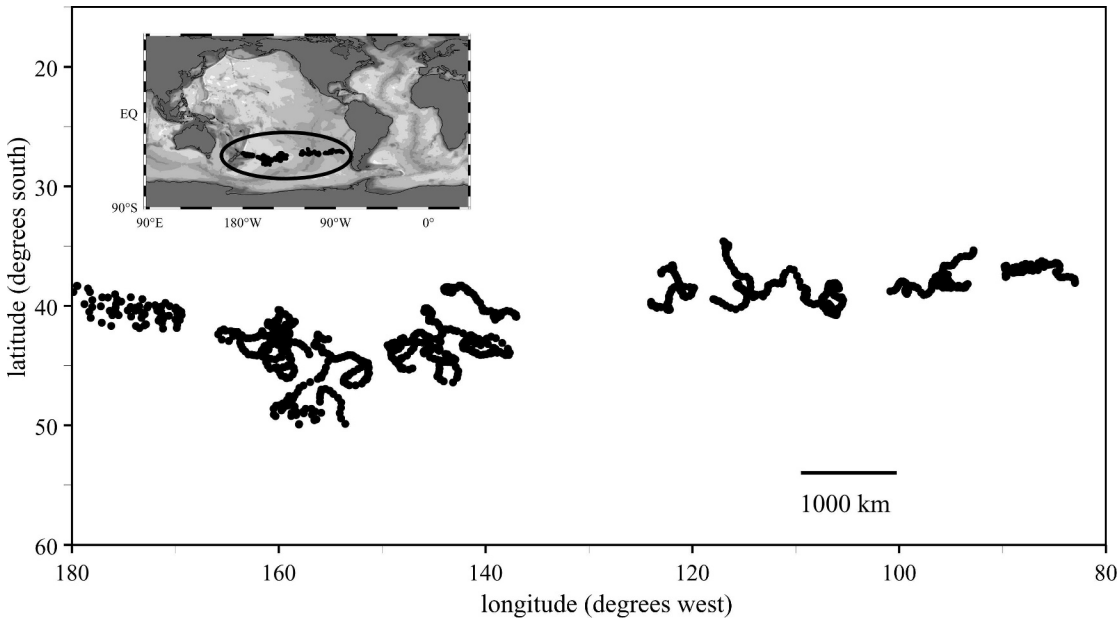

Fig. 1. Locations of all float profiles from the 18 Argo floats.

seasonal ecological cycle for the majority of the region occupied by the floats is relatively unstudied. Bradford-Grieve et al. (1999) and references therein give more information on the pelagic ecosystem structure in this region.

Argo float data—In early April 2007, float profiles were retrieved from the U.S. Global Ocean Data Assimilation Experiment (USGODAE). Two floats were immediately removed from the data set due to unreasonably high changes in O_2 concentration registered at 1,900 m. Each of the 18 floats selected (Table 1) measured 66–72 profiles and typically recorded 69 or 70 depth intervals during each profile, giving a total of 1,212 stations with 83,816 measurement points.

The CTD data were quality controlled by an Argo data center before dissemination. For temperature, salinity, and pressure, only those values with a 'good' QC flag were used. At the time of data retrieval there was no QC performed by the Argo data center on oxygen data. Upon visual examination of the oxygen profiles, only a few values were deemed obvious outliers and removed. To preserve the effect of averaging a large number of oxygen measurements to obtain what we consider a 'true' mean value, further removal of oxygen data was avoided. The primary QC procedures employed in our analysis involved examination of the 1,900-m time series of each float. We compared the Argo data to a gridded field of historical oxygen measurements at 1,900 m (Fig. 2). The 1,900-m grid was produced from the WOCE and Reid-Mantyla data sets (Schlitzer 2007) using cubic triangulation in Matlab. A correction offset specific to each float was applied based on the difference between the float's first 1,900-m measurement and the WOCE climatology (Table 1). A second correction specific to each float was used to account for sensor drift. The slope (least-squares regression) of all available 1,900-m oxygen measurements vs. time for a particular float was applied to each oxygen measurement at all depths. As shown in the Results section, the drift correction usually constituted $<10\%$ of the remineralization signal between 50 m and 200 m.

Satellite data—Monthly satellite NPP was obtained from the NOAA Southwest Fisheries Science Center's CoastWatch Program (http://coastwatch.pfeg.noaa.gov/). This data was based on Sea-viewing Wide Field-of-view Sensor (SeaWiFS) Photosynthetically Active Radiation (PAR) and Chlorophyll and Pathfinder Sea Surface Temperatures (SST), as described in Behrenfeld and Falkowski (1997). Absolute accuracy was not reported, but variability between two different productivity models averaged over the South Pacific was $\sim$25% (Behrenfeld et al. 2005). Satellite NPP was taken as the average of the five monthly values from December through April (*see* Data analysis) reported at the location of each float during the midpoint of this period (i.e., February). In many cases, fewer than 5 months of satellite data were available. Satellite NPP, corresponding to Argo EP rates, was obtained by averaging the two to five available satellite NPP monthly data points over the same periods used to calculate EP. The positioning and averaging scheme used for satellite NPP was simplistic but effective for demonstrating the feasibility of a new method for estimating EP from profiling float data. Future studies focusing more vigorously on spatial variability in the e-ratio will require a more sophisticated scheme for synchronizing satellite pixels to float profiles. For the 18 floats on average, monthly satellite NPP was reported for 13 months of the 15 months between December 2005 and March 2007. A monthly composite NPP over the deployment area was calculated by combining all available monthly NPP data. As described in the next section, the annual NPP was used to extend the

Table 1. Float name, date, location, number of profiles (Prof), difference between the first measured 1,900 m oxygen concentration and the WOCE dataset, 1,900-m changes measured by Argo, and 1,900-m changes measured by Argo plus expected changes from the WOCE data.

Float no.	First date/location	Last date/location	Prof (*n*)	1,900-m 1st prof - WOCE (μmol O_2 kg^{-1})	[a]1,900 m (μmol O_2 kg^{-1} yr^{-1})	[b]1,900 m (μmol O_2 kg^{-1} yr^{-1})
	12 Nov 2005	28 Mar 2007				
3900333	39.2°S, 113.1°W	40.8°S, 106.1°W	66	−4.8	−5.1	7.0
	14 Nov 2005	30 Mar 2007				
3900334	38.8°S, 100.8°W	35.4°S, 92.8°W	66	−1.2	−11.2	−8.1
	04 Nov 2005	28 Mar 2007				
3900344	39.4°S, 118.0°W	35.1°S, 116.5°W	67	−6.3	−6.1	−1.9
	06 Nov 2005	30 Mar 2007				
3900345	39.0°S, 107.0°W	38.6°S, 105.8°W	67	5.9	−11.3	−11.4
	09 Nov 2005	02 Apr 2007				
3900346	38.5°S, 95.0°W	37.4°S, 95.9°W	66	−2.5	−3.6	−2.5
	11 Nov 2005	27 Mar 2007				
3900348	38.1°S, 83.0°W	37.6°S, 89.7°W	66	−3.1	−2.1	−5.5
	24 Jul 2003	11 Aug 2005				
5900421	41.9°S, 173.5°W	38.6°S, 178.4°W	72	3.7	−1.4	−0.2
	27 Oct 2005	27 Mar 2007				
5901043	43.7°S, 161.0°W	41.3°S, 158.4°W	68	−3.7	−6.9	−2.2
	27 Oct 2005	28 Mar 2007				
5901044	44.1°S, 157.0°W	41.6°S, 159.3°W	68	−6.2	−5.6	−7.8
	02 Nov 2005	26 Mar 2007				
5901045	43.6°S, 159.3°W	40.9°S, 160.0°W	67	1.1	−5.8	−3.8
	03 Nov 2005	27 Mar 2007				
5901046	44.6°S, 155.2°W	49.9°S, 153.6°W	67	−1.6	−0.3	−3.6
	28 Oct 2005	29 Mar 2007				
5901047	44.7°S, 151.9°W	42.8°S, 155.2°W	68	−5.2	−5.9	−2.3
	29 Oct 2005	30 Mar 2007				
5901048	44.0°S, 145.9°W	44.5°S, 143.0°W	68	1.4	−4.3	−3.6
	04 Nov 2005	28 Mar 2007				
5901049	44.4°S, 148.1°W	40.5°S, 145.9°W	67	−1.8	−5.9	−20.8
	30 Oct 2005	31 Mar 2007				
5901050	42.5°S, 141.5°W	42.3°S, 144.2°W	68	−15.7	−5.3	−9.1
	05 Nov 2005	29 Mar 2007				
5901051	43.6°S, 144.6°W	45.2°S, 147.1°W	67	−8.2	−4.4	3.0
	07 Nov 2005	30 Mar 2007				
5901052	40.9°S, 137.1°W	38.8°S, 143.9°W	67	−12.1	−6.0	−13.5
	09 Nov 2005	02 Apr 2007				
5901054	39.7°S, 124.0°W	37.3°S, 123.0°W	67	−9.7	−8.2	−6.9
	Average ± 95% CI		67	−3.9 ± 2.5	−5.5 ± 1.3	−5.2 ± 2.9

[a] Rate of change in 1,900 m Argo oxygen measurements.
[b] Rate of change from column 6 plus expected changes due to natural gradients.

subannual Argo EP rates to annual rates by assuming EP and NPP were coupled throughout the year.

Data analysis—All calculations presented here are based on the ratio $C_{org}:O_2 = 0.688$, reported by Anderson and Sarmiento (1994), from an analysis of the GEOSECS dataset. As indicated in the introduction, export production was calculated using the Argo oxygen concentrations in the region directly below the mixed layer. The rate of oxygen consumption at a particular depth was determined to be the slope of oxygen concentration vs. time for the period from December to April. We calculated $EP_{50–200}$ as the integral of the rates between depths of 50 m and 200 m, which was numerically equivalent to the slope of the 50–200-m oxygen inventory vs. time. The time and depth intervals were selected after examination of float profiles and some preliminary calculations of EP. At 35–45°S in the Pacific Ocean, the period from December to April represents a shallow mixed layer during peak production. During this time, the 50-m depth is consistently deeper than the mixed layer for all floats, and the slopes became indistinguishable from noise below ~200 m. As shown below (Figs. 3, 16b), the upper limit of 50 m corresponded to the mean summertime Z_c. Annually, significant EP occurs well below 200 m and throughout the year. The $EP_{50–200}$ values calculated for individual floats from December to April are extended to 900 m ($EP_{50–900}$) using a composite profile obtained by binning all float data. For comparison with reported annual values, this remineralization profile is converted to carbon and extended to an annual rate, assuming that seasonality was identical to the NPP annual composite. Due to temperature effects, oxygen concentration was used rather than oxygen anomaly (oxygen concentration − oxygen solubility) or percent saturation. In

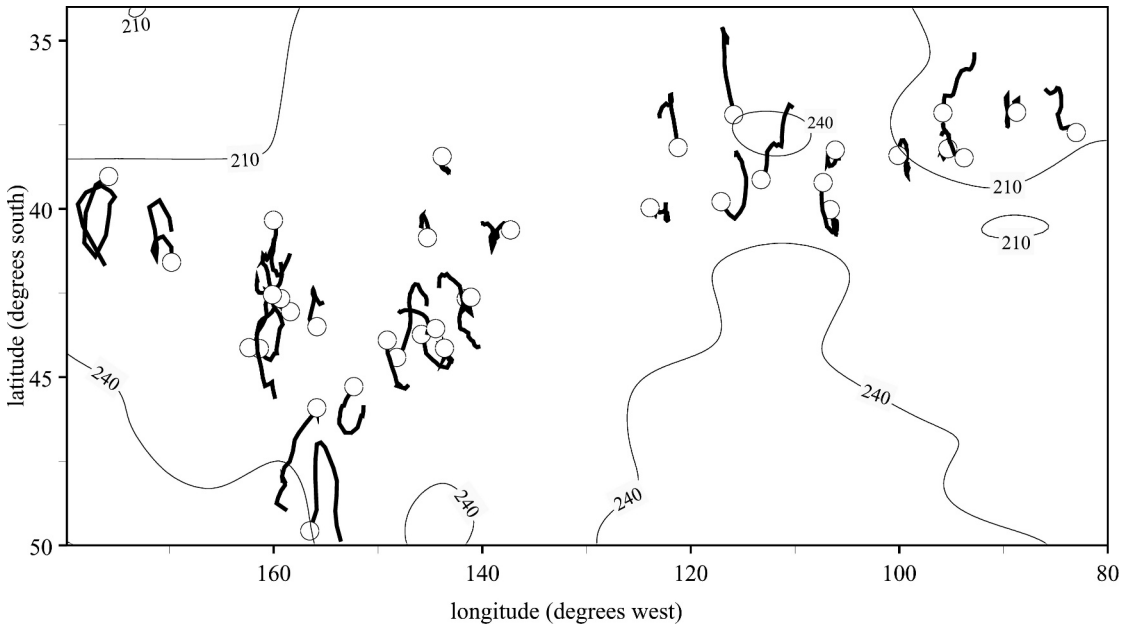

Fig. 2. Gridded contour at 1,900 m based on WOCE oxygen data. Traces indicate the float trajectories from December to April (two traces per float), with the first December profile shown as an open circle.

an effort to reduce the effect of vertical excursions in the thermocline and halocline, EP was also calculated based on slopes of oxygen concentration on isopycnals and integrated over the mean depths of the isopycnals. This approach gave slightly noisier results, not significantly different than the calculation at fixed depths (*see* Results).

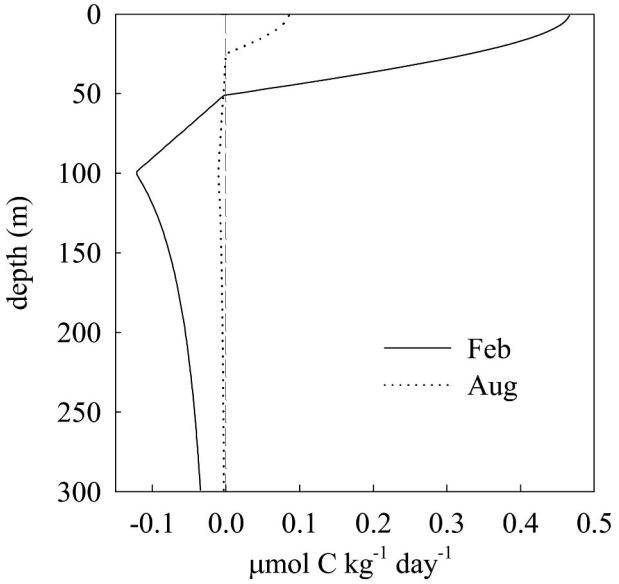

Fig. 3. Productivity-remineralization profiles used in the biogeochemical model. The profile labeled 'Feb' is for a typical day in the summer when Z_c = 50 m and the NCP seasonal amplitude is 1.8× the mean yearly NCP. The profile labeled 'Aug' is for a typical day in the winter when Z_c = 25 m and the NCP seasonal amplitude is 0.5× the mean yearly NCP. As described in the text, the ratio $C_{org}:O_2$ = 0.688 is used to convert between oxygen and organic carbon.

We recognized that the particle export ratio (pe-ratio) and the steady-state ratio of NCP : NPP (e-ratio) were not strictly equivalent due to processes involving dissolved organic matter and EP-NCP decoupling (Dunne et al. 2005; Brix et al. 2006), e.g., some fraction of the EP observed by the floats must be fueled by DOM. However, these distinctions fall within the uncertainty of the present data set, so we did not distinguish between the pe-ratio and the e-ratio.

For each of the 36 Argo EP values, an estimate of the e-ratio can be calculated directly as the quotient of Argo EP and satellite NPP. An alternative calculation of the e-ratio is a model II least-squares regression of EP vs. NPP for all floats and years, where the slope is interpreted as the e-ratio. For the regression analysis it was assumed that the e-ratio is relatively constant over a range of different NPP and EP and over the area occupied by the floats. Based on fig. 4.1.7(b) in Sarmiento and Gruber (2006), this assumption was marginally valid. Superimposing the 18 Argo floats on their contour plot, the e-ratio was expected to range from ~0.12 to 0.17, generally increasing moving southwest from 35°S, 90°W to 45°S, 160°W.

In addition to EP, NCP, can be estimated based on the oxygen cycle. Riser and Johnson (2008), analyzed two floats located in the northern (22°N, 156°W) and southern (22°S, 120°W) Pacific subtropical gyres. The data from the floats provided positive rates of change in oxygen concentration within the shallow oxygen maximum (SOM) over ~300-d periods. At the higher latitudes (~40°S) considered in this study, the rate of change in oxygen levels within the SOM did not exhibit a consistent increase, so although the formation of an SOM was indicated by data from most floats, it was not directly attributable to photosynthesis. We attempted to resolve the relative roles of physics vs. biology in the formation of the SOM, using a physical-biogeochemical model.

Model—The Price-Weller-Pinkel (PWP) model of mixed-layer physics (Price et al. 1986), modified to include net community metabolism (Musgrave et al. 1988; Spitzer and Jenkins 1989), was used to estimate the magnitude of NCP at 45°S, 144°W. The model was initiated using the first profile of data from float A (*see* Results) and then driven by the 6-hr daily heat budget, winds, and precipitation data obtained from the NCEP/NCAR Reanalysis (Kalnay et al. 1996). The lower boundary of the model was set using interpolated Argo data. O_2 solubility, and gas transfer velocity were calculated following Garcia and Gordon (1992) and Wanninkhof (1992), respectively. Simple approximations of the cool skin effect and bubble contributions were included following Sarmiento and Gruber (2006) and Woolf and Thorpe (1991). Magnitudes of biologically driven changes in O_2 were distributed over depth using a half-cosine function above the compensation depth, a differentiated 'Martin' power function (Martin et al. 1987) below 100 m, and a straight line connecting the compensation depth to the 100-m value (Fig. 3). A half-cosine function was chosen based on the assumption that productivity is greatest at the surface in the region of the floats (Burkholder and Burkholder 1967). The differentiated Martin function was used to model the consumption zone, rather than a straight line as originally used by Musgrave et al. (1988), because we assumed that the majority of remineralization in the consumption zone was fueled by sinking particles and this function describes the remineralization rate profile more accurately than a straight line. The straight line between Z_c and 100 m was necessary to provide a continuous, smooth transition from net production to net respiration, rather than an abrupt jump from Z_c to the first (and largest negative) value of the power function. Also, the differentiated power function can produce unreasonably high remineralization rates when extrapolated to depths $<\sim$100 m. The productivity half-cosine function was the type C profile described by Musgrave et al. (1988):

$$\mathrm{NCP}_z\left(\mathrm{mol\,m^{-3}yr^{-1}}\right)=\frac{\mathrm{NCP}\left(\mathrm{mol\,m^{-2}yr^{-1}}\right)\pi}{2Z_c}\cos\left(\frac{z\pi}{2Z_c}\right) \quad (1)$$

with a maximum at the surface, extinguishing at the compensation depth, Z_c. The least-squares solution between the model and Argo data was found using a two-step iterative process. First, a vertical turbulent diffusivity term, K_z, was found by minimizing the sum of squared temperature residuals between the model and Argo measurements using a non-linear least-squares algorithm. Next NCP was found using an identical approach to that for K_z, except squared oxygen residuals were minimized. The log-log intercept of the remineralization function was set such that 90% of the NCP is remineralized between 50–300 m. Seasonality of NCP is expressed as a sine function with a February maximum and August minimum

$$\mathrm{NCP}_t=\mathrm{NCP}\left[1+A\cdot\sin\left(\frac{2\pi t}{t_{\mathrm{yr}}}+\varphi\right)\right] \quad (2)$$

where t is year-second and t_{yr} is s yr^{-1}. The amplitude (A = 0.51) and phase (φ = −0.29) of Eq. 2 were set using least squares minimization to match the annual composite NPP (Fig. 4). The time lag between production and export increases with depth. In the upper few hundred meters particle transit time ($\sim$1–3 d; Berelson 2002) was shorter than the measurement interval (7 d) of the floats. Therefore, in the model, we assumed no phase lag between NPP, NCP, and EP, which appears to have been reasonable in the upper 200 m (*see* Results). The compensation depth Z_c was calculated using the mean compensation irradiance reported by Siegel et al. (2002), I_c = 3.3 W m^{-2}. Radiative heating was applied with the typical double exponential function for oceanic water type IA (Paulson and Simpson 1977). The type IA attenuation coefficient for the blue-green wavelengths (0.05 m^{-1}) was used to calculate Z_c as $Z_c = -\ln(I_c/I_o)/0.05$. The equation of Morel (1988) used by Siegel et al. (2002), gave a similar attenuation coefficient (0.045–0.060 m^{-1}) for the range of Chl *a* (0.1–0.2 mg m^{-3}) at 40°S in the Pacific Ocean (Falkowski et al. 1998).

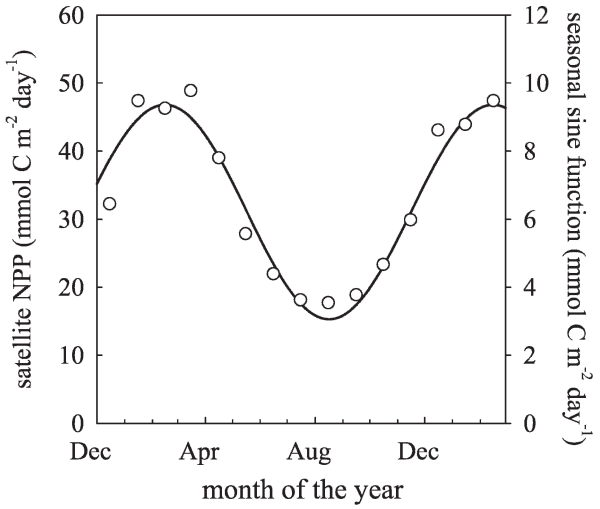

Fig. 4. Monthly binned satellite NPP and the sine function used to drive seasonality in the PWP model.

Results

1,900-m data—The relationship between all float measurements at 1,900 m and their corresponding historical values from the WOCE grid is shown in Fig. 5. Upon deployment, the majority of the float oxygen values were negatively biased. The average difference between the first 1,900-m float measurement and the WOCE grid was −4 μmol kg^{-1}, ranging from −16 μmol kg^{-1} to +6 μmol kg^{-1} (Table 1). Several floats exhibited an initial drop of $\sim$5 μmol kg^{-1} during the first 1–2 months of deployment. All calculations presented here began after this conditioning period.

Observed changes in the 1,900-m float record are due to a combination of sensor drift and natural oxygen gradients at 1,900 m. From the series of float locations reported for each profile, expected oxygen changes along a 1,900-m grid, generated using the WOCE database (Fig. 2), were produced. As seen in Fig. 6 the floats registered an overall negative trend not found in the grid. A general lack of

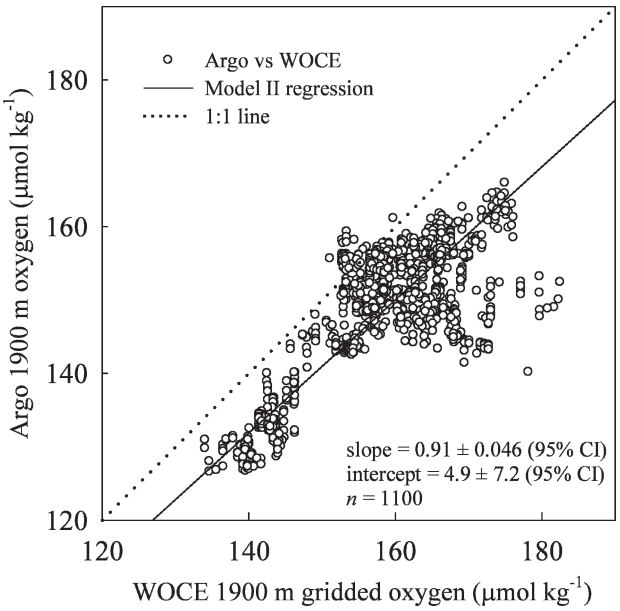

Fig. 5. Model II regression showing the relationship between all float measurements and the WOCE grid at 1,900 m.

coincidence between many abrupt features in the grid and those observed in the float data indicates that the grid is not well constrained due to the sparse coverage in many regions. Including the expected natural gradients shown in Fig. 6b in the drift corrections increased the variance of the drift corrections roughly five-fold (Table 1). Consequently, including the expected gradients in the sensor drift correction resulted in increased noise in the oxygen rates used to determine export production. The rates reported here were corrected for sensor drift using a straight line fitted by least squares to the data measured by Argo at 1,900 m, with no correction for natural gradients (Table 1, column 6). At present, it is not clear whether such corrections should have been applied directly as concentrations or as a percentage of the measured concentration. The concentration-based corrections used in this study would be amplified 2–3× at the surface if applied as percentages.

Annual cycles observed by Argo—We examined the seasonal dynamics of two floats, 5901048 and 3900333, henceforth referred to as floats A and B, respectively. Physical properties and oxygen (adjusted as described above) measured from 0 m to 300 m illustrate the typical variability of water column structure over an annual cycle (Fig. 7). The deepest mixing occurs in August–September (Fig. 7a,b), preceding the highest surface oxygen concentrations. For float A, a distinct SOM developed in December and persists through April. For several floats the SOM reached below 50 m, but in general the December–April oxygen rates of change were negative within the SOM, indicating its demise rather than formation. As described previously, 50 m is considered to be an appropriate upper bound for the estimation of remineralization rates.

Figure 8 shows typical annual cycles of temperature and oxygen observed in the upper 200 m in the South Pacific.

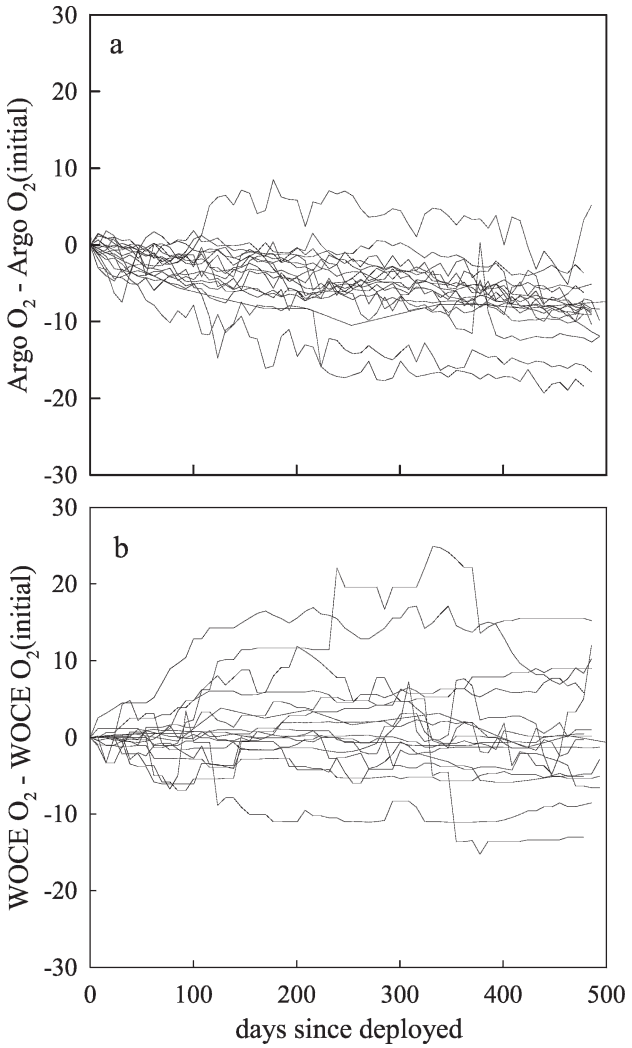

Fig. 6. Changes in (a) float oxygen measured at 1,900 m and (b) WOCE grid, based on changes in float position.

The surface oxygen anomaly (Fig. 8b) peaks in early summer due to the combined effects of heating and net community production. (In Fig. 8b, the accuracy of the oxygen anomaly may be biased low [possibly due to post factory calibration drift] but the cycle of the anomaly exhibited the expected behavior.) By mid-summer outgassing, driven by seasonal heating, overtakes production and the surface oxygen anomaly begins to decrease. Mixed layer deepening in the late fall reinforces the already decreasing anomaly. The 50–200 m oxygen inventory (Fig. 8c) exhibits a ventilation-respiration cycle, as described above. When the mixed layer reaches its maximum in August–September, the 50–200 m oxygen inventory is ventilated. As the mixed layer shoals, beginning in November, the inventory decreases throughout the summer until the next fall. Export production for our study was determined from the inventory decrease (*see* next section).

Water mass changes may have resulted in a negative value of EP calculated from the data of some floats. For example, float A yielded two positive EP values (Fig. 8c) and float B yielded a positive EP during its first year and a

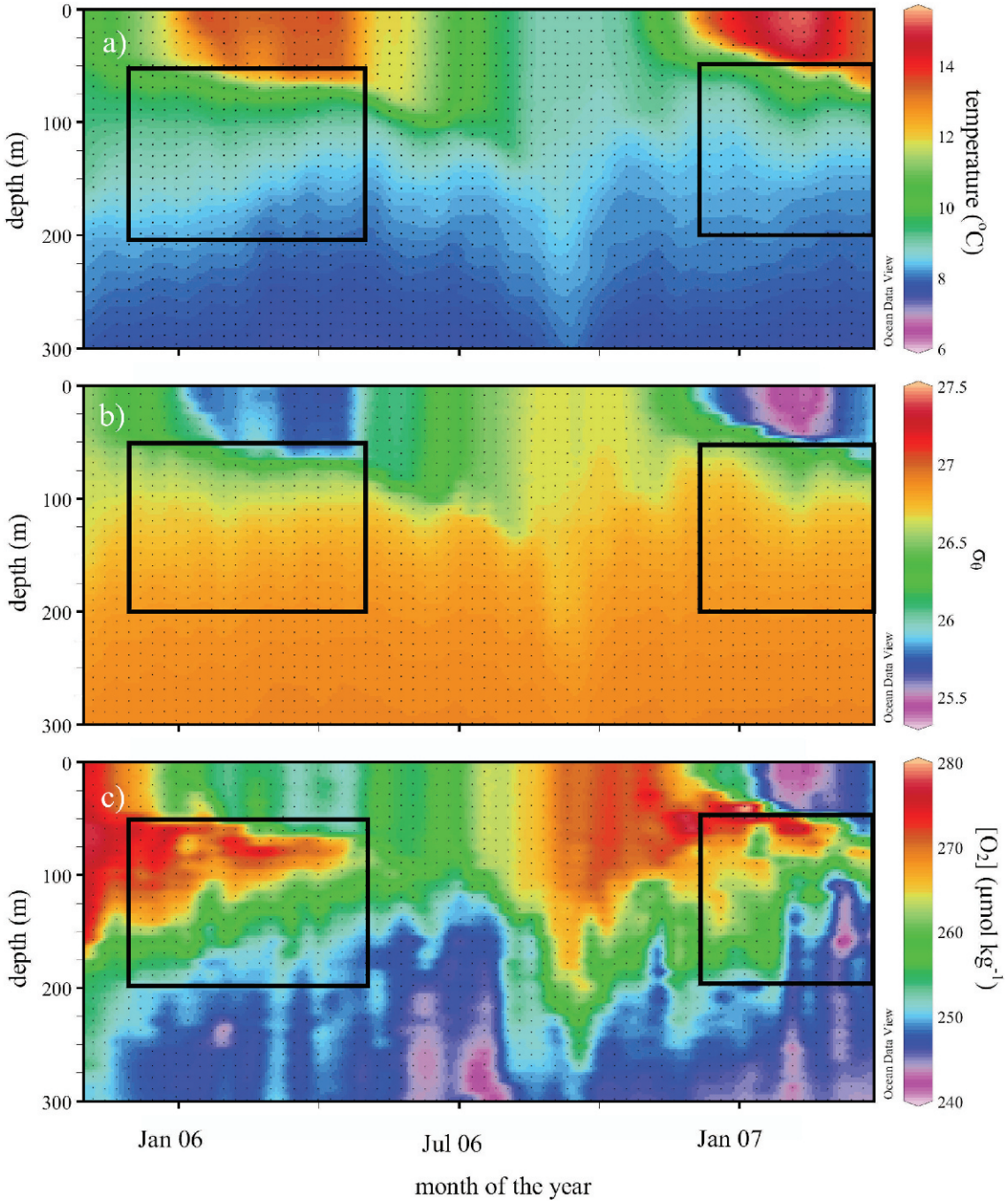

Fig. 7. Time series contours of (a) temperature, (b) potential density, and (c) corrected oxygen for float A. Measurement points are indicated by small dots. Rectangles denote the depth and time intervals used to calculate remineralization rates. Contours prepared with Ocean Data View (Schlitzer 2007).

negative EP in its second year (Fig. 9). The 50–200 m oxygen inventory from data from float B showed an abrupt increase in February 2007 (Fig. 9). The source of this irregularity became evident upon examination of vertical profiles in the same season of different years. The seasonal changes in vertical structure illustrate the late summer to fall oxygen drawdown in the upper 200 m of the water column (Fig. 10). The accompanying changes in temperature and salinity were due to both seasonal variability and movement of the float into different water masses. In Fig. 10 the first two rows of profiles contain a winter profile and its preceding and following summer profiles of temperature, salinity, and oxygen data for the two floats. In the first row, data from float A showed a fairly similar vertical structure between March 2006 and 2007. In both years, the 50–200 m oxygen inventory showed a consistent decrease from December to April. The salinity profiles from float A showed very similar seasonal behavior,

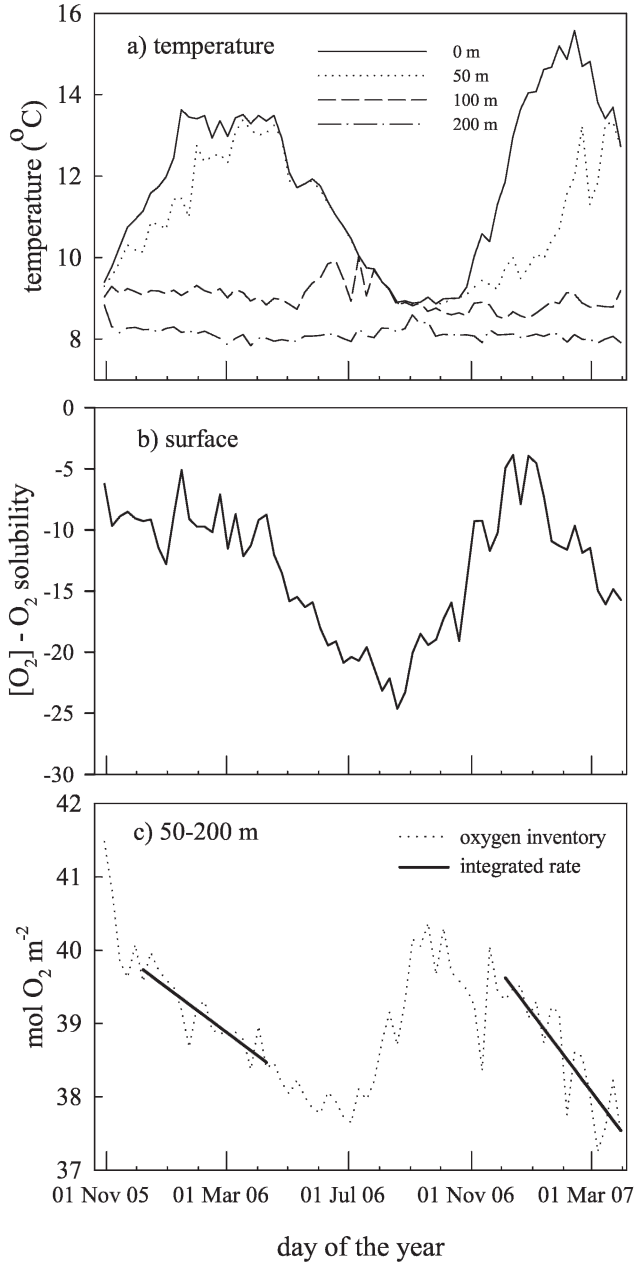

Fig. 8. Seventeen month time series of (a) temperature at 0 m, 50 m, 100 m, and 200 m, (b) surface oxygen anomaly, and (c) 50–200-m oxygen inventory for float A. The solid lines in (panel c) represent the calculated oxygen utilization rates.

indicating that the float remained in relatively homogenous water. In contrast, the data from float B showed considerable changes in vertical structure between summer profiles. From 50 m to 350 m, the float B February 2007 oxygen profile is greater than the September 2006 profile, opposite the expected trend. During this time, the salinity decreased from 0 m to 350 m, opposite the behavior of the first year. A comparison to the nearby WOCE line P18S explains the observed trends in both salinity and oxygen. The WOCE profiles shown in the third row of the figure are adjacent stations measured in March 1994 along 103°W at 33.5°S and 34.0°S. These stations show the abrupt change

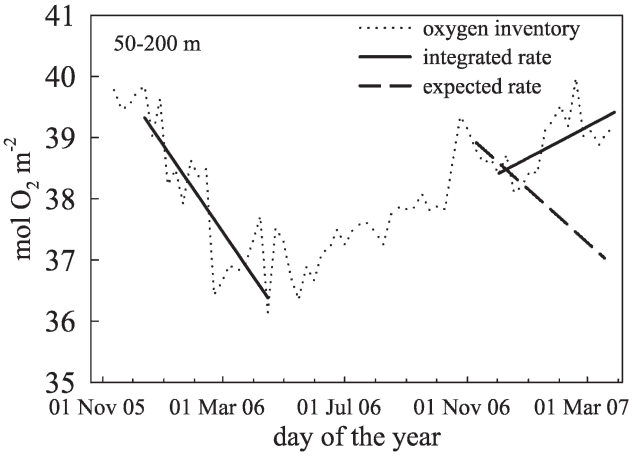

Fig. 9. Fifty-meter to two-hundred-meter oxygen inventory for float B. As described in the text, in Feb 2007, the float crossed the STF, causing an anomalous rise in the integrated values resulting in a negative calculated EP (solid line with positive slope). The dashed line represents the expected trend.

observed between 0.5° of latitude at the STF. From December 2006 to March 2007, float B traveled from 40.1°S to 40.8°S, probably crossing the STF. The trend of increasing oxygen and decreasing salinity in the upper 500 m as the STF is traversed from north to south is therefore the most likely cause of the anomalous rise in the 50–200-m oxygen inventory observed in February 2007 by float B. Of the 36 integrated rates, eight $EP_{50–200}$ values and two $EP_{50–900}$ values were negative. For the regressions and averages reported in this study, all 36 EP values were retained to avoid biasing the mean. This choice was based on the assumption that the mean changes in EP driven by water mass variability tended to cancel as the number of floats increases (e.g., southward floats crossing the STF are balanced by northward floats).

The 36 trajectories from December through April (Fig. 2) showed little systematic movement of floats in any direction and, in fact, most exhibited heading changes of greater than 180° during the 5-month period. These features, however, do not absolve the analysis presented here from the biases shown in Fig. 10. Unfortunately, due to seasonal variability, gridded WOCE data such as those used for float corrections (Figs. 2, 6) were not reliable for detecting potential water mass changes in the surface ocean. As the number of floats with oxygen sensors increases, errors due to float migration through surface gradients will become easier to identify. This potential drawback must be given a high priority in all future work based on the methods presented here.

We explored techniques to account for water mass changes. The rates of change in oxygen concentration between the surface and 900 m were similar when plotted at fixed depths or mean depths of isopycnals (Fig. 11). Some smoothing of the rate profiles was evident when constant density was used, but because integrating isopycnal rates of change over mean depths did not lead to significantly different results, we report rates based on fixed depths only. Temperature–salinity–oxygen relationships were also ex-

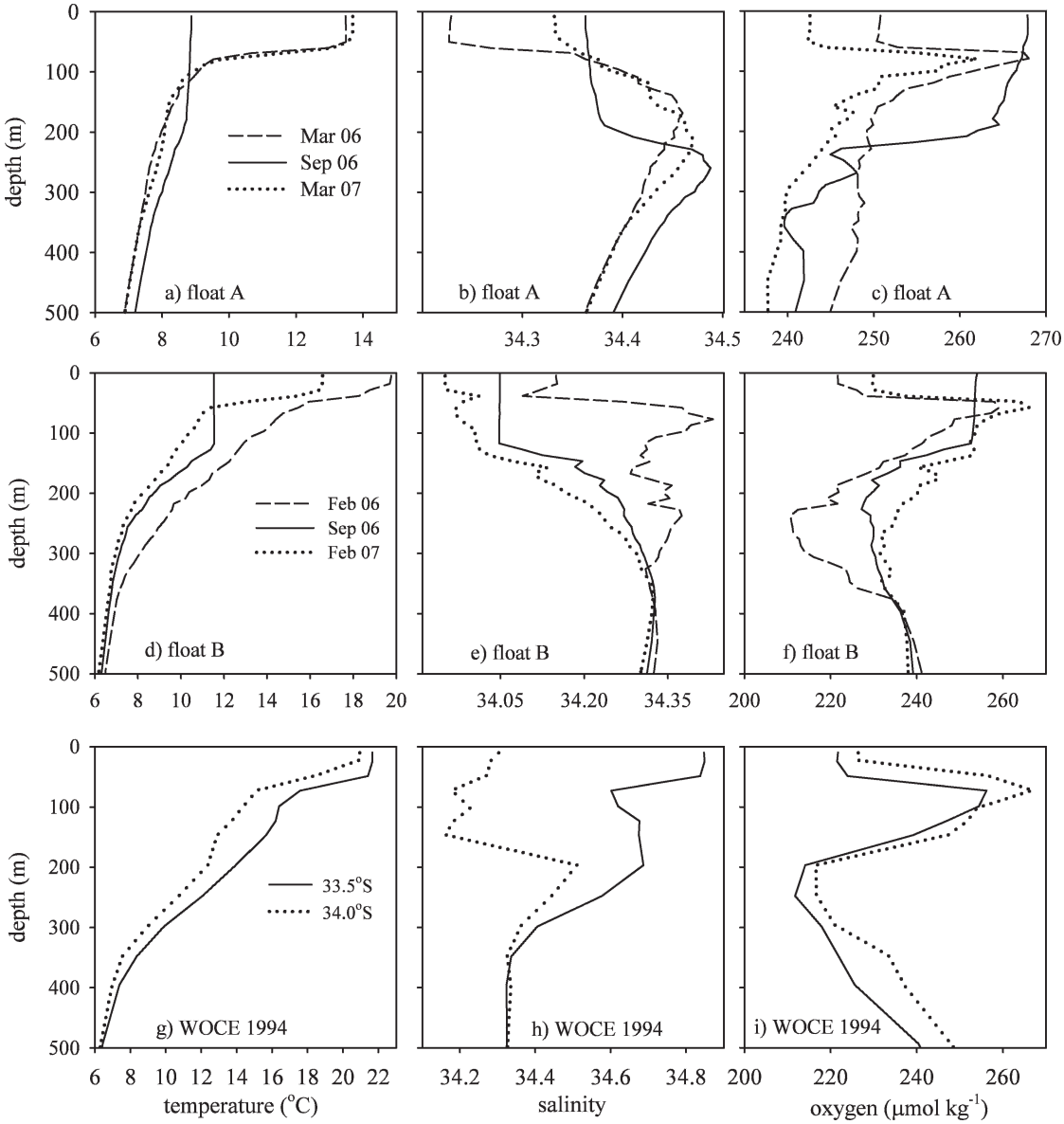

Fig. 10. (a, d, g) Temperature, (b, e, h) salinity, and (c, f, i) oxygen profiles from (panels a, b, c) float A, (panels d, e, f) float B, and (panels g, h, i) WOCE line P18S. (Panels a-f) are seasonal profiles from floats and (panels g-i) show successive profiles during March 1994 along 103°W at 33.5°S and 34.0°S.

amined, but no clear pattern appears to exist above ~500 m. Although we found no simple correction approach that could be applied to a single float, a sufficient number of contiguous floats would potentially supply the information necessary on lateral chemical gradients and transport velocities to account for advection and float migration.

Oxygen utilization rate (OUR)-based metabolism estimates—Based on the monthly averages, satellite NPP was 11.4 mol C m^{-2} yr^{-1} in the region occupied by the 18 floats. The oxygen rate of change at each depth interval for the period December 2005–April 2006 and December 2006–April 2007 is shown in Fig. 12 (n = 36). A single-rate profile exhibits considerable variability and the signal : noise typically reaches 1 at ~200 m (Fig. 11). Although a single float cannot reliably observe 4-month remineralization signals below 200 m, averaging all 36 profiles produced a remarkably realistic remineralization profile to 900 m (Fig. 13). As described in the Methods section, the oxygen rates (Fig. 12) were converted to annual carbon units for Fig. 13. The vertical attenuation of particle flux is described reasonably well by a Martin function (Martin et al. 1987) with b exponent between −0.20 and −0.10, depending on the shallow depth cutoff used (e.g., 200 m vs. 100 m). A double exponential flux attenuation function (Armstrong et al. 2002) gave a fit indistinguishable from the Martin function, which is not surprising, considering the relatively narrow depth range used for the fit. Due to vertical changes in sinking rate, mineral ballast effects, and degree of lability the

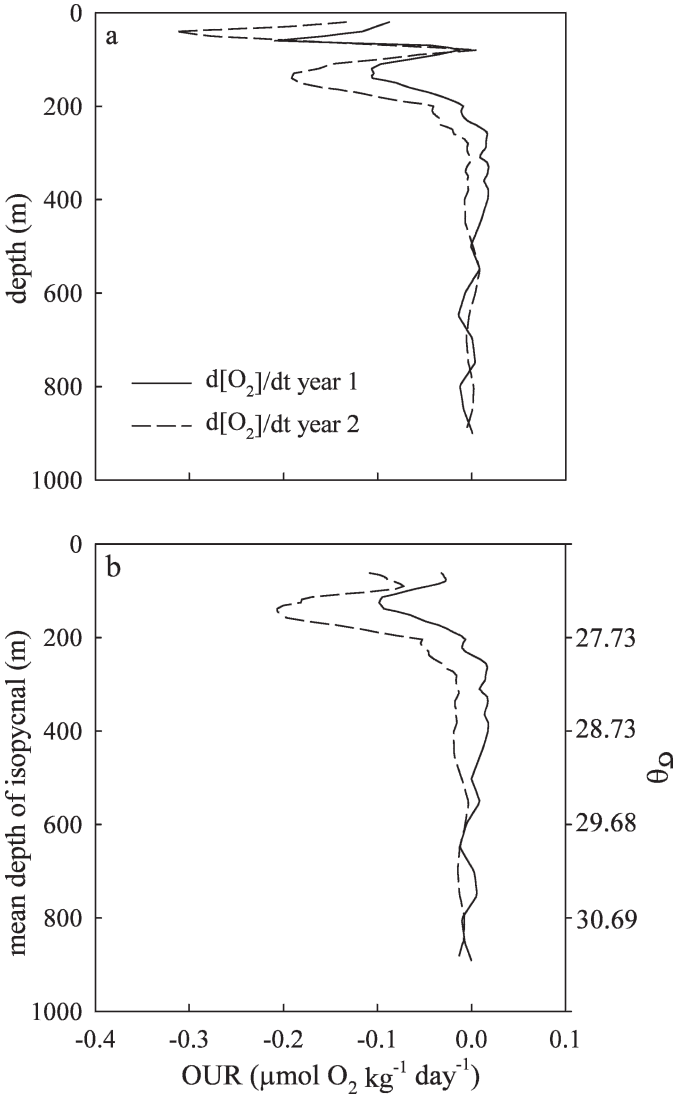

Fig. 11. Oxygen utilization rate for float A at (a) fixed depths and (b) mean depths of isopycnal surfaces. In (panel b) rates are plotted linearly vs. depth to the shallowest depth where σ_θ did not outcrop, and σ_θ is indicated on the right y-axis. Rates are calculated from December 2005 to April 2006 (year 1) and December 2006 to April 2007 (year 2).

use of a double exponential formulation of particle flux often proves superior to the simpler power law when fit to data spanning the entire water column (e.g., 100–5,000 m). Because our 4-month rates were limited to the upper 1,000 m it was not possible here to compare different flux attenuation parameterizations where the differences occur primarily at depth. Shown in Fig. 13 are the 36 rates averaged on 100-m intervals with error bars corresponding to 95% confidence intervals. Although the lower bound of the 95% CIs approach zero below 400 m, the systematically positive mean values suggest a real signal that could be better established by including a larger number of profiles. The oxygen-based remineralization rates based on data from the floats agree well with the apparent oxygen utilization (AOU)-based rates from the hydrographic surveys of Feely et al. (2004), and both are considerably higher than the trap-

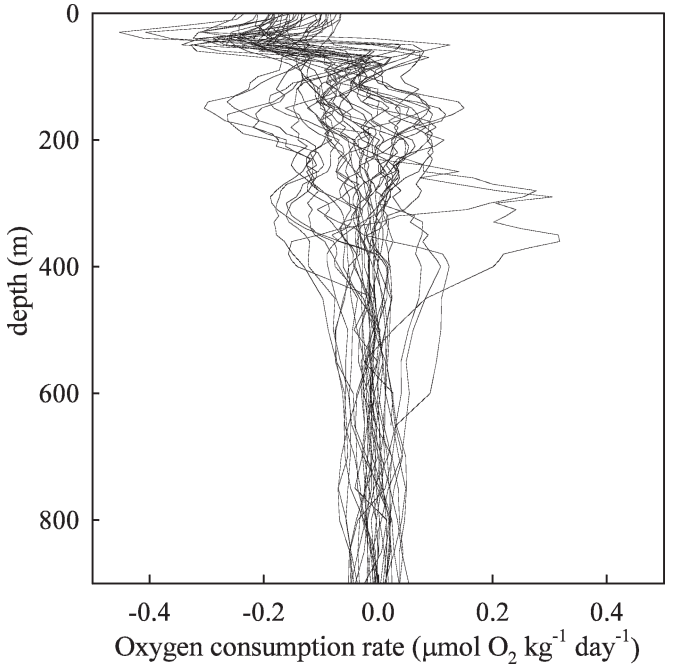

Fig. 12. The 36 oxygen rates of change from 0 m to 900 m for the period December–April.

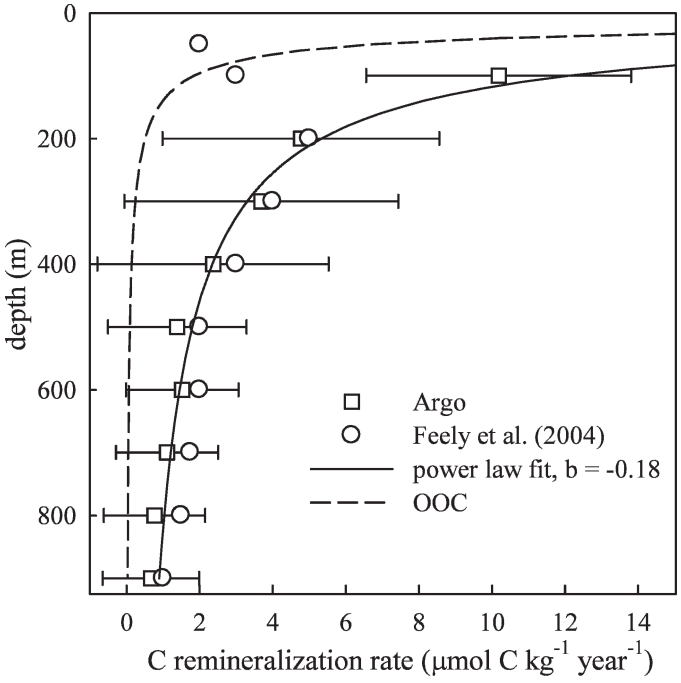

Fig. 13. Argo annual remineralization rates calculated from December to April rates extended to 12 months using the satellite composite monthly seasonality (*see* text) and calculated as the average of the 36 rate profiles shown in Fig. 12 and binned in 100-m intervals (open squares with 95% CI); Data from Feely et al. (2004; open circles). Also shown is a differentiated Martin power function ($R_{100} = 12.1$, $b = -0.18$), and the open ocean composite (OOC) of Martin et al. (1987).

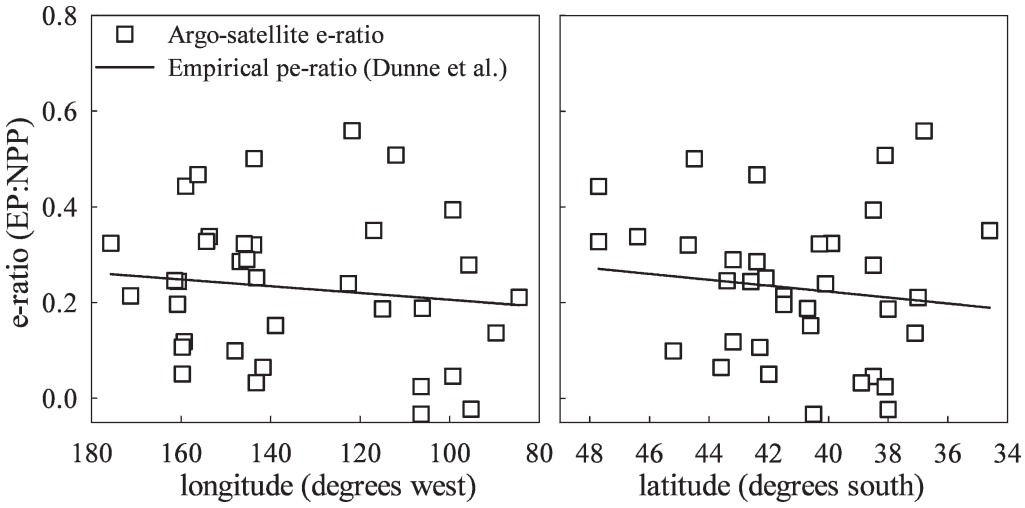

Fig. 14. The e-ratio, EP : NPP, for each point measured by Argo and Satellite (open squares). The average of the 36 points is 0.23 ± 0.04. Also shown are the trends (solid lines) predicted for the pe-ratio calculated using the empirical relationship between NPP, temperature, and euphotic zone depth given by Dunne et al. (2005).

based Open Ocean Composite of Martin et al. (1987). The sensitivity of the *b* exponent to errors in OUR and active transport by zooplankton is addressed below (*see* Discussion).

The average of the 36 EP values, based on integrated remineralization rates over the two 5-month periods from December 2005–April 2006 and December 2006–April 2007, was 10.7 ± 2 mmol C m^{-2} d^{-1} (95% CI). The average satellite NPP corresponding to the 36 EP values was 46 ± 4 mmol C m^{-2} d^{-1} (95% CI). The point-by-point ratio of Argo EP to satellite NPP was 0.23 ± 0.04 (n = 36, 95% CI). The Argo-satellite e-ratio, plotted vs. latitude and longitude (Fig. 14), exhibited a slight, barely statistically significant slope (trend lines not shown), decreasing from west to east and from south to north. The error in this slope was on the same order as the slope itself, but the trends in both directions agree in sign with those predicted for the pe-ratio by the empirical relationship of Dunne et al. (2005; Fig. 14). Although these trends were scarcely resolved by either the Argo-satellite relationship or the Dunne et al. relationship, we suggest that such trends would be detectable with a greater density of floats equipped with oxygen sensors. To test the hypothesis that EP and NPP are correlated in this region, we plotted EP vs. NPP and determined the e-ratio as the slope (Model II least squares regression) 0.20 ± 0.2 (95% CI; Fig. 15). The large error in the least squares-based e-ratio indicates that the e-ratio was not constant over the area occupied by the floats and supports the fact that NPP and EP need not correlate. Including the effect of float movement in the sensor drift correction (*see* above) did not significantly change the calculated e-ratio; the point-by-point e-ratio changed by +0.04 and the model II e-ratio changed by <0.01.

Model results—The Argo-constrained 1-D model gives K_z ~1.6 × 10^{-4} m^2 s^{-1} and NCP ~2.5 mol C m^{-2} yr^{-1}, using ~17 months of float A data from October 2005 through March 2007. This number was similar to estimates of annual ^{14}C-based productivity from incubations performed in the STF (Burkholder and Burkholder 1967). As discussed by Spitzer and Jenkins (1989), the model's K_z represented processes in addition to diapycnal mixing (e.g., wind mixing) and was necessarily larger than the diapycnal diffusivity rate alone. The residual matrix consisted of 1,005 measurements in the upper 150 m (the deepest winter mixed layer depth) spanning 516 d. The RMS of the temperature residual matrix for K_z and the oxygen residual matrix for NCP is 0.7°C and 10 μmol kg^{-1}, respectively. The modeled NCP for float A over the two production

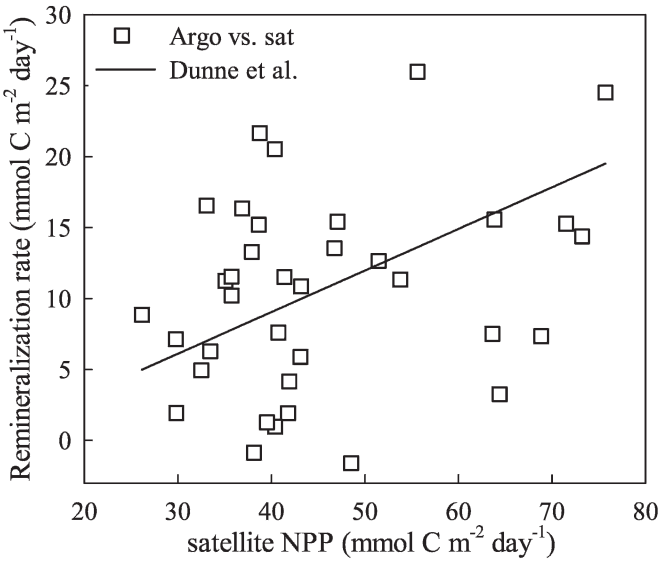

Fig. 15. The relationship between Argo remineralization rate EP (50–200 m) and satellite NPP. The slope (Model II, major axis regression) of EP vs. NPP is 0.2 ± 0.2 (95% CI), indicating a weak relationship between EP and NPP. Also shown is the trend in particle EP calculated using the empirical relationship between NPP, temperature, and euphotic zone depth given by Dunne et al. (2005).

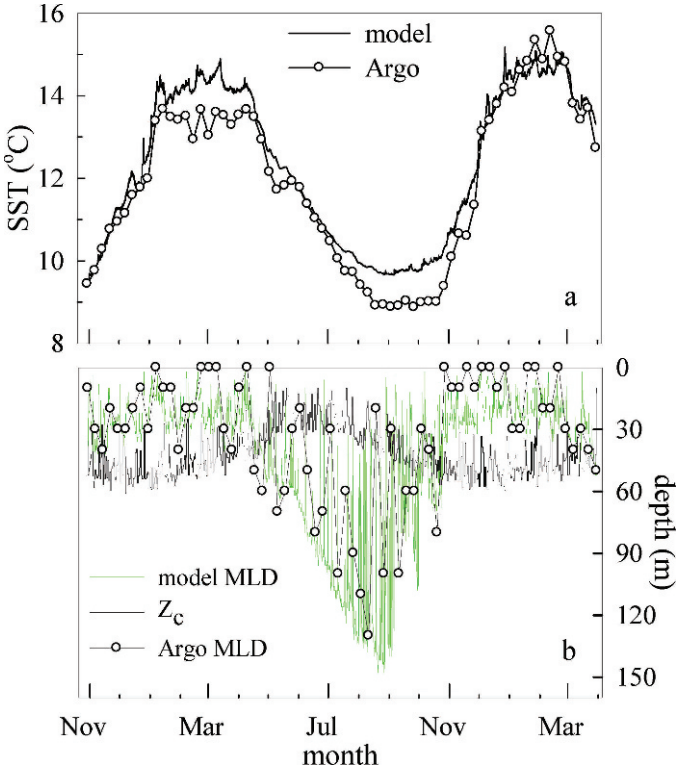

Fig. 16. Results of the measured and modeled mixed layer physics for float A. (a) Sea-surface temperature, (b) mixed-layer depth, and compensation depth, Z_c.

seasons (year 1 = 6.6 mmol C m^{-2} d^{-1}; year 2 = 9.9 mmol C m^{-2} d^{-1}) agreed reasonably well with the integral of the binned remineralization rates between 50 m and 900 m (EP_{50-900} = 9.0 mmol C m^{-2} d^{-1}).

Figures 16 and 17 compare the results of the PWP model with Argo measurements. The PWP physics produced reasonable agreement between temperature and mixed-layer depth (Fig. 16a,b), although the model produced surface temperatures that were too high during March 2006 and too low during the following winter. Errors of this magnitude are not uncommon for a 1-D model and may have resulted from biases in the NCEP/NCAR heat budget, float migration, advection or, most likely, a combination of all of these factors. Annual oxygen cycles at the surface (Fig. 17a) were out of phase with temperature as expected. Upon deployment, the float recorded a surface oxygen value 4.5 μmol kg^{-1} lower than the equilibrium saturation value of 286.5 μmol kg^{-1}, and measured a value 1.4 μmol kg^{-1} higher than the corresponding 1,900 m WOCE grid point. To reduce model spin-up, an initial 4.5 μmol kg^{-1} correction was applied to the Argo data for the initial PWP profile and the post-model least-squares fit. As discussed earlier, a correction of +4.3 μmol kg^{-1} yr^{-1} was applied to all float A O_2 data (Table 1). In the model, surface oxygen is always within ± 3% of saturation. The model predicted 9 months of supersaturated surface water from November to June with an efflux of −4.0 mol O_2 m^{-2} or −3.9 mol O_2 m^{-2} with the air injection parameter. In the winter, an intense period of undersaturated conditions persisted from July to September,

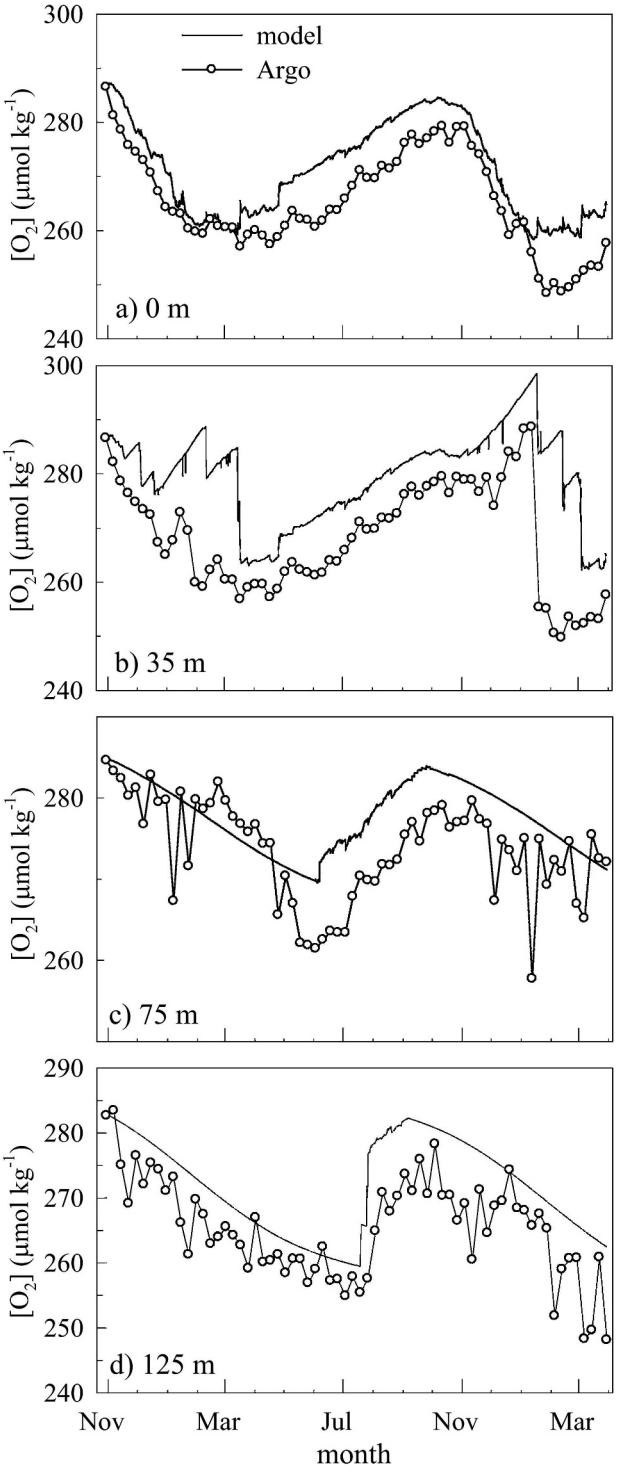

Fig. 17. Comparison of Argo oxygen measurements with results from the PWP model for float A at (a) 0 m, (b) 35 m, (c) 75 m, and (d) 125 m.

resulting in an influx of +1.3 mol O_2 m^{-2} or +1.7 mol O_2 m^{-2} with air injection. The annual flux of the model with and without air injection was −2.2 mol O_2 m^{-2} and −2.7 mol O_2 m^{-2}, respectively, corresponding to a loss (to the atmosphere) of magnitude similar to the photosynthetically produced oxygen.

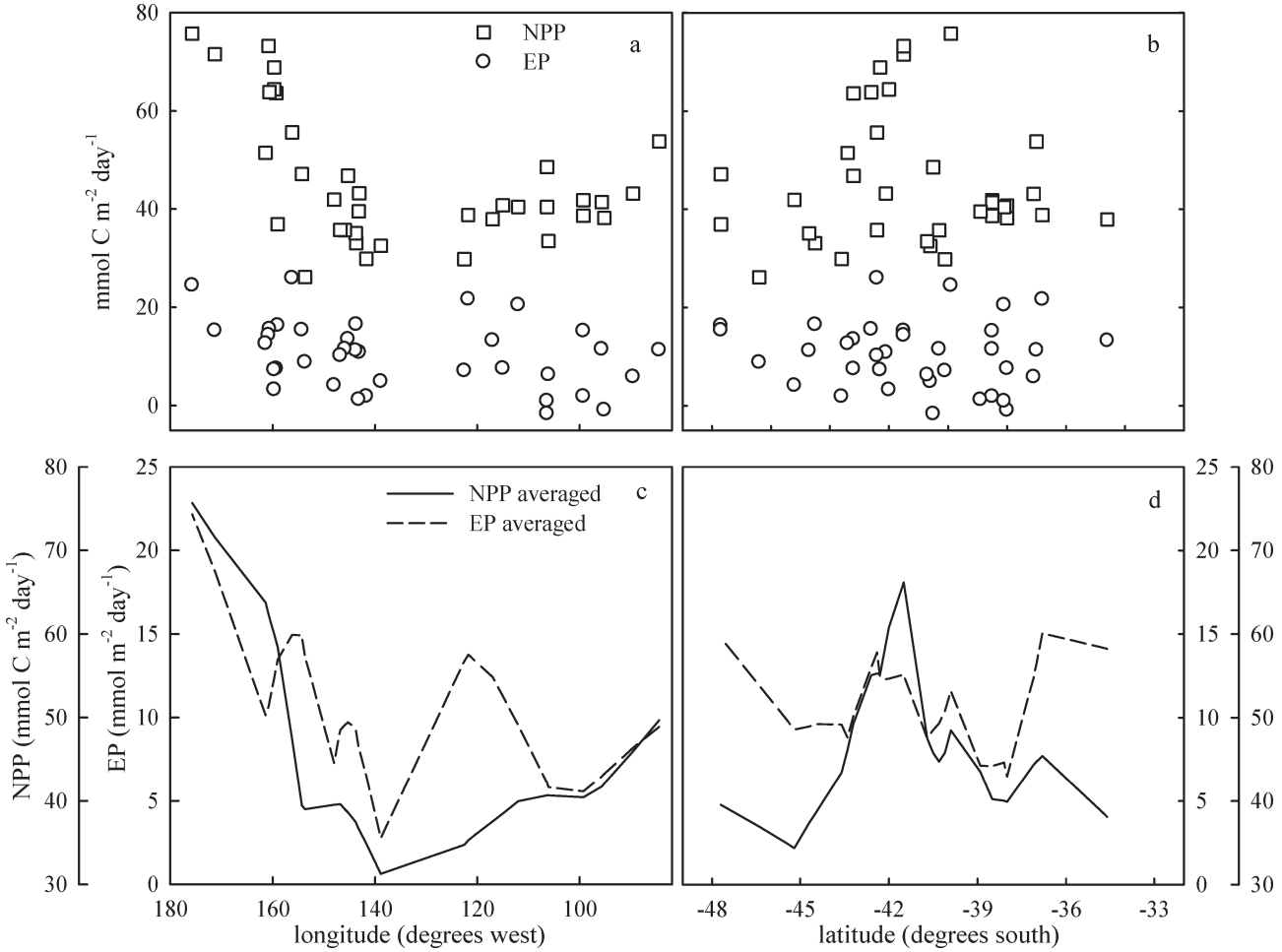

Fig. 18. December–April NPP and EP (same data as in Fig. 14) plotted vs. (a) longitude and (b) latitude. (c) and (d) show the smoothed data for (panels a and b), respectively. The averages in (c) and (d) were calculated using locally weighted regression (lowess) with a smoothness parameter of 0.3. Correlation coefficients for the smoothed data in (c) and (d) are 0.61 and 0.42, respectively.

The SOM provided in data provided by float A centered at ~75 m (Fig. 7c). During the summer, oxygen concentration decreased in the SOM (Fig. 17c) rather than increasing as hypothesized by Schulenberger and Reid (1981). This counterintuitive process is attributed to the location of the compensation depth Z_c (Fig. 16b). Biologically driven accumulation of O_2 occurs during the summer at depths between the mld and Z_c when the mixed-layer depth is shallower than the compensation depth. This precept was supported by comparing the 35-m vs. 75-m oxygen values during December–March (Fig. 17b,c). When the mld was <35 m, oxygen accumulated at 35 m. In general, the model overestimated the buildup of O_2; although a distinct 35-m O_2 increase was observed from December 2006 to mid-January 2007 that the model reproduceds quite well (Fig. 17b). The greater separation between Z_c and mld found at lower latitudes results in a more obvious and consistent accumulation of oxygen within the SOM, supporting Schulenberger and Reid's hypothesis (Riser and Johnson 2008). We concluded that, at 40°S, however, the summertime formation of an SOM was due mainly to the heating and solubility-driven loss of O_2 in the mixed layer and respiratory consumption of O_2 below the SOM, not from accumulation of biologically produced O_2.

The ventilation-respiration pattern is quite clear at 125 m (Fig. 17d). When water mass changes were minimal, as described above, the consumption of oxygen between Z_c and ~200 m provided a robust signal on subannual time scales (e.g., -10 μmol O_2 kg^{-1} over 4 months at 125 m). The model contained no phase lag between production and export. The absence of lag between the model and measured oxygen suggests that production and export remain coupled within the 7-d resolution of the floats throughout the year in the near-surface ocean at this location. In this system, export is not dominated by a pulse of sinking carbon in the fall.

Spatial trends—Several broad, corresponding trends in NPP and EP were discernable when the data were smoothed with a running average (Fig. 18). The averaged data showed increases in production and export west of 150°W as the New Zealand shelf was approached (Fig. 18c). A similar but smaller increase appeared to the east of 100°W in the direction of the Chilean coast (Fig. 18c). Meridionally, NPP and EP appeared to peak

around 42°S, perhaps indicating increased productivity in the vicinity of the STF.

Discussion

The results reported here involve several, somewhat contentious, constants. Most important, the conversion between oxygen and carbon-based rates of production and remineralization hinged on accurate ratios of $C_{org}:O_2$. As stated earlier, we adopted $C_{org}:O_2 = 0.688$. Other values of this ratio, such as the classic Redfield ratio of 0.768 or the regional value reported by Li and Peng (2002) of 0.578 would result in 11% higher and 16% lower estimates of EP and NCP, respectively. The 50–200-m depth interval used to calculate remineralization rates was carefully selected, as described in the Methods section. The 50-m upper limit corresponded closely to the summer Z_c (Fig. 16b) and the 200-m lower limit corresponded to the depth where the magnitude of O_2 consumption over 4 months was indistinguishable from other sources of variability. Oxygen rates of change were also calculated for each float over the same time period, but at varying upper and lower bounds. In doing so, we found that the rates based on the 50–200-m depth interval produced the highest correlation between EP and NPP (Fig. 15). Based on the binned rates of change in oxygen levels reported in this work and by others (Jenkins and Goldman 1985; Feely et al. 2004), there exists a discrepancy between sediment trap-derived and OUR-derived b values. Because of the great importance of accurately describing the vertical nature of remineralization, a thorough understanding the source of this inconsistency should motivate future work.

Following the notation used by Martin et al. (1987), b values are typically expected (although not required) to be negative in the range of approximately -1.28 to -0.59 (Berelson 2001). A larger b value (negative exponent closer to zero) represents a more efficient transfer of organic matter to depth. The b exponent found by fitting the Argo oxygen data (-0.18) was considerably higher (closer to zero) than the upper limit of ~ -0.6, established in a number of sediment trap surveys (Berelson 2001).

A simple sensitivity analysis was performed to examine the effect of oxygen measurement errors on the b exponent of the Martin function that was estimated from float data. The mean error value of ± 1.3 mmol O_2 m^{-3} yr^{-1} for deep oxygen concentration measurements (Table 1), converted to C using $C_{org}:O_2 = 0.688$, corresponds to ± 0.9 mmol C m^{-3} yr^{-1}. Applying this error as a systematic offset of 1 mmol C m^{-3} yr^{-1} to the data shown in Fig. 13 resulted in a 150–300% change in b, depending on which data are used in the fit (binned vs. unbinned depth intervals). The error in our estimate of b was therefore too large to establish a statistical difference between the value $b = -0.18$ and a b value of -0.5 to -0.6. However, the float-derived value of b did appear to be larger than typical values derived from sediment trap profiles, which were generally much smaller than this (Berelson 2001). For a more thorough discussion of errors in the b exponent see Primeau (2006).

Basin scale mapping of compensation depth (Siegel et al. 2002) and the annual O_2 cycle (Najjar and Keeling 1997) demonstrated that Z_c deepens equatorially and seasonally (with insolation) and that the amplitude of seasonal oxygen cycles generally increases with latitude. Najjar and Keeling (1997) defined the "oxygen nodal depth" as the depth where the annual oxygen cycle exhibits a minimum in amplitude along with a phase shift, indicating a change in conditions from the production zone to the consumption zone. The climatology of Najjar and Keeling (1997) did not resolve zonal differences in the annual oxygen cycle in the South Pacific, but the increasing density of direct observations of the annual oxygen cycle in this region may soon allow a comparison of zonal trends in the Argo oxygen-based nodal depth and satellite-derived compensation depth.

Due to the lack of comparative EP data in the southern Pacific Ocean it is not yet clear whether there is a fundamental difference between oxygen-based and trap-based remineralization rates. As discussed by Buesseler et al. (2007*b*), the nature of particle flux attenuation varies with location. This observation is thought to reflect ecosystem differences and is not ostensibly related to the magnitude of particle flux (Primeau 2006). The trap data presented by Buesseler et al. suggest that, at a given location, transfer efficiency remains relatively constant despite natural intra-seasonal variability in NPP. If the methods are comparable, then this region of the South Pacific actually exhibited ultra-high transfer efficiency for carbon flux to depth, relative to areas where traps have been deployed (e.g., Martin et al. 1987; Berelson 2001; Buesseler et al. 2007*b*).

A variety of explanations may account for the differences in b exponents derived from OUR vs. sediment traps. Lateral gradients in organic matter or oxygen could bias the trap-based vs. OUR-based b exponents either positively or negatively. The trap-based b exponent would be more negative than the OUR-based b exponent if trapping efficiency of the sediment trap exhibited a systematic variability with depth (Yu et al. 2001), suffered significant undersampling errors (Buesseler et al. 2007*a*), or if zooplankton actively transported significant amounts of organic matter such that particulate carbon is ingested at shallow depths and then respired at greater depths (Steinberg et al. 2000). Seasonal variability may also have led to differences between the ARGO 4-month average and the duration of sediment trap experiments.

Alternatively, much of the difference might be reconciled by zooplankton carbon transport. The effect of active transport by zooplankton was estimated using the classic Open Ocean Composite carbon flux function where $b = -0.86$ and carbon export flux at 100 m = 1.53 mol C m^{-2} yr^{-1} (Martin et al. 1987). The zooplankton "short-circuit" was applied by removing a percentage of the flux at 100 m, remineralizing it equally between 300 m and 600 m, and refitting the b exponent to the new data. The refitted data would represent the signal measured by oxygen sensors. For a fitted depth range of 200–900 m, redistribution of 5%, 10%, 15%, and 20% of the 100-m flux raised the b exponent from -0.86 to -0.62, -0.44, -0.30, and -0.20,

respectively. Respiration of 20% of the carbon ingested at 100 m at greater depths would completely reconcile b values of -0.2 from oxygen measurements with b values of -0.86 from sediment traps. Martin et al. noted a similar discrepancy between the VERTEX sediment trap-based remineralization rates and the Sargasso Sea AOU-based rates of Jenkins and Goldman (1985), which suggests that this difference may be widespread. Thus, the large sensitivity of the b parameter to zooplankton transport of a relatively small fraction of the particulate carbon suggests that differences in b values may also result because our models of carbon transport are too simplistic. Sinking carbon ingested by zooplankton that actively avoid traps may be respired at depths greater than the site of ingestion. Steinberg et al. (2000) suggest that this is a relatively minor process near the Bermuda Atlantic Time Series station. However, it may be more important at sites with a more pronounced seasonal carbon cycle.

The effects of several model input parameters on the modeled NCP were investigated. First, we noted that the value $K_z = 1.6 \times 10^{-4}$ m^2 s^{-1} was at the high end of the range typically used in PWP models. Alternative approaches (e.g., adjusting the heat budget terms within expected error ranges, recalibrating the model's profile if a diagnostic passes a certain limit) were explored to find better agreement between the thermal cycle and modeled temperature. However, these results were not pursued because such methods require a departure from objectivity. And so, advection, and float drift were folded into the rather high K_z value used in the model. In the sensitivity analysis, the two most critical model parameters, K_z and Z_c, affect NCP by up to 50%. Adding air injection to the model raised the NCP from 2.5 mol C m^{-2} yr^{-1} to 3.0 mol C m^{-2} yr^{-1}. A stochastic wind component resulted in a 6% change in K_z and a 2% change in NCP. The percentage of NCP remineralized in the upper 300 m ($\sim$80–90%), variations in the seasonal distribution of productivity, the Martin function exponent, and gas transfer velocity all gave $\leq$5% change in NCP. Bubble processes clearly play an important role (Lazarevich et al. 2004; Hamme and Emerson 2006), but adding this parameterization seriously degraded the model-float fit driving the modeled surface oxygen much higher than observed and forcing the minimization to higher NCP values. Alternatively, one could tune the K_z to mix the additional oxygen deeper, but using oxygen to constrain K_z is probably a poor choice (Spitzer and Jenkins 1989). The calculation algorithm minimizes the residuals between two surfaces and, therefore, overlaying and lining up surface features (i.e., Z_c, mld) proved to be as important as matching up exact concentrations.

As pointed out by Musgrave et al. (1988) and Spitzer and Jenkins (1989), the level to which oxygen provides a constraint on PWP NCP is limited because much of the biologically produced oxygen signal is lost through gas exchange. This finding was reaffirmed by Hamme and Emerson (2006), who stressed the importance of air bubbles. In an effort to circumvent and minimize the problems identified in these studies, we have shifted our focus to the consumption zone. Instead of attempting to constrain NCP with oxygen measurements in the mixed layer or above the euphotic zone, we used annual data from the surface to the deepest wintertime mixed-layer depth. The result is that a majority of the data used in the least-squares fit was located beneath the continuously ventilated production zone. Consequently, the least-squares solution of NCP depended to a greater extent on oxygen measurements below the mixed layer, and contributions from the poorly understood terms related to gas exchange and bubble injection were minimized.

In addition to ocean metabolism, oxygen sensors on profiling floats provide information on several important physical processes. Most notably, deep mixing has been observed in the north Atlantic (Körtzinger et al. 2004). The potentially great contributions of Argo oxygen to studies of ocean circulation, the apparent reduction now occurring in the ocean's oxygen inventory, and the carbon budget have been recognized (Joos et al. 2003). Estimating air–sea flux directly from Argo measurements is not yet possible because the sensors operate with accuracy equal to the range of disequilibrium observed in most surface waters ($\sim\pm5$ μmol kg^{-1}). Due to sparse data coverage, small air–sea disequilibrium, and annual magnitude near zero globally, determination of the global oxygen air–sea flux is an extremely challenging task (Garcia and Keeling 2001). The disagreement between Argo-measured and PWP-modeled surface oxygen anomaly exemplifies this difficulty. Better than 2% accuracy is required to resolve the correct sign of the gas flux and even higher accuracy ($\sim$0.5%) is necessary for meaningful flux calculations. However, as demonstrated here, Argo oxygen data provide a powerful constraint on models that consider the short time scales necessary to capture air–sea flux processes. Furthermore, the prospect of using Argo oxygen to constrain a large scale inverse model is exciting because it would certainly contribute to the elusive explanation of modeled vs. measured atmospheric potential oxygen (Battle et al. 2006). Improvement in sensor performance is currently being addressed (Gruber et al. 2007). For example, the oxygen optode (Tengberg et al. 2006) has received a great deal of attention and has already been tested on Argo floats (Körtzinger et al. 2005).

In this study we have shown that oxygen sensors on profiling floats successfully record the intra-annual signal due to remineralization of exported organic matter. Extrapolating from the 18 floats discussed here, the benefits of an Argo fleet outfitted with oxygen sensors are considerable. Our results suggest that this achievement would provide spatial coverage of the e-ratio orders of magnitude better than those presently available.

References

Anderson, L. A., and J. L. Sarmiento. 1994. Redfield ratios of remineralization determined by nutrient data analysis. Global Biogeochem. Cycles **8:** 65–80.

Armstrong, R. A., C. Lee, J. I. Hedges, S. Honjo, and S. G. Wakeham. 2002. A new, mechanistic model for organic carbon fluxes in the ocean based on the quantitative association of POC with ballast minerals. Deep-Sea Res. II **49:** 219–236.

Battle, M., and others. 2006. Atmospheric potential oxygen: New observations and their implications for some atmospheric and oceanic models. Global Biogeochem. Cycles **20:** GB1010, doi:10.1029/2005GB002534.

Behrenfeld, M. J., E. Boss, D. A. Siegel, and D. M. Shea. 2005. Carbon-based ocean productivity and phytoplankton physiology from space. Global Biogeochem. Cycles **19:** GB1006, doi:10.1029/2004GB002299.

———, and P. G. Falkowski. 1997. A consumer's guide to phytoplankton primary productivity models. Limnol. Oceanogr. **42:** 1479–1491.

Berelson, W. M. 2001. The flux of particulate organic carbon into the ocean interior: A comparison of four U.S. JGOFS regional studies. Oceanography **14:** 59–67.

———. 2002. Particle settling rates increase with depth in the ocean. Deep-Sea Res. II **49:** 237–251.

Bradford-Grieve, J. M., and others. 1999. Pelagic ecosystem structure and functioning in the Subtropical Front region east of New Zealand in austral winter and spring 1993. J. Plankton Res. **21:** 405–428.

Brix, H., N. Gruber, D. M. Karl, and N. R. Bates. 2006. On the relationships between primary, net community, and export production iin subtropical gyres. Deep-Sea Res. II **53:** 698–717.

Buesseler, K. O., and others. 2007*a*. An assessment of the use of sediment traps for estimating upper ocean particle fluxes. J. Mar. Res. **65:** 345–416.

———, and others. 2007*b*. Revisiting carbon flux through the ocean's twilight zone. Science **316:** 567–570.

Burkholder, P. R., and L. M. Burkholder. 1967. Primary productivity in surface waters of the South Pacific Ocean. Limnol. Oceanogr. **12:** 606–617.

Chaigneau, A., and O. Pizarro. 2005. Surface circulation and fronts of the South Pacific Ocean east of 120°W. Geophys. Res. Lett. **32:** L08605, doi:10.1029/2004GL022070.

DeGrandpre, M. D., T. R. Hammar, and C. D. Wirick. 1998. Short-term pCO_2 and O_2 dynamics in California coastal waters. Deep-Sea Res. II **45:** 1557–1575.

———, R. Wanninkhof, W. R. McGillis, and P. G. Strutton. 2004. A Lagrangian study of surface pCO_2 dynamics in the eastern equatorial Pacific Ocean. J. Geophys. Res. **109:** C08S07, doi:10.1029/2003JC002089.

Dunne, J. P., R. A. Armstrong, A. Gnanadesikan, and J. Sarmiento. 2005. Empirical and mechanistic models for the particle export ratio. Global Biogeochem. Cycles **19:** GB4026, doi:10.1029/2004GB002390.

Emerson, S., P. Quay, D. Karl, C. Winn, L. Tupas, and M. Landry. 1997. Experimental determination of the organic carbon flux from open-ocean surface waters. Nature **389:** 951–954.

———, C. Stump, B. Johnson, and D. M. Karl. 2002. In situ determination of oxygen and nitrogen dynamics in the upper ocean. Deep-Sea Res. I **49:** 941–952.

Falkowski, P. G., R. T. Barber, and V. Smetacek. 1998. Biogeochemical controls and feedbacks on ocean primary production. Science **281:** 200–206.

Feely, R. A., C. L. Sabine, R. Schlitzer, J. L. Bullister, S. Mecking, and D. Greeley. 2004. Oxygen utilization and organic carbon remineralization in the upper water column of the Pacific Ocean. J. Oceanogr. **60:** 45–52.

Garcia, H., and L. Gordon. 1992. Oxygen solubility in seawater: Better fitting equations. Limnol. Oceanogr. **37:** 1307–1312.

———, and R. F. Keeling. 2001. On the global oxygen anomaly and air-sea flux. J. Geophys. Res. **106:** 31155–31166.

Gehlen, M., L. Bopp, N. Emprin, O. Aumont, C. Heinze, and O. Ragueneau. 2006. Reconciling surface ocean productivity, export fluxes and sediment composition in a global biogeochemical ocean model. Biogeosciences **3:** 521–537.

Grob, C., O. Ulloa, W. K. W. Li, G. Alarcón, M. Fukasawa, and S. Watanabe. 2007. Picoplankton abundance and biomass across the eastern South Pacific Ocean along latitude 32.5°S. Mar. Ecol. Prog. Ser. **332:** 53–62.

Gruber, N., and others. 2007. The Argo-oxygen program: A white paper to promote the addition of oxygen sensors to the International Argo float program. http://www-argo.ucsd.edu/o2_white_paper_web.pdf.

Hamme, R. C., and S. R. Emerson. 2006. Constraining bubble dynamics and mixing with dissolved gases: Implications for productivity measurements by oxygen mass balance. J. Mar. Res. **64:** 73–95.

Hooker, S. B., and C. R. McClain. 2000. The calibration and validation of SeaWiFS data. Prog. Oceanogr. **45:** 427–465.

Jenkins, W. J., and J. C. Goldman. 1985. Seasonal oxygen cycling and primary production in the Sargasso Sea. J. Mar. Res. **43:** 465–491.

Johnson, K. S., L. J. Coletti, and F. P. Chavez. 2006. Diel nitrate cycles observed with in situ sensors predict monthly and annual new production. Deep-Sea Res. I **53:** 561–573.

———, J. A. Needoba, S. C. Riser, and W. J. Showers. 2007. Chemical sensor networks for the aquatic environment. Chem. Rev. **107:** 623–640.

Joos, F., G.-K. Plattner, T. F. Stocker, A. Körtzinger, and D. W. R. Wallace. 2003. Trends in marine dissolved oxygen: Implications for ocean circulation changes and the carbon budget. EOS **84:** 197–204.

Kalnay, E., and others. 1996. The NCEP/NCAR 40-year reanalysis project. Bull. Amer. Meteor. Soc. **77:** 437–471.

Karl, D. M., E. A. Laws, P. Morris, P. J. L. B. Williams, and S. Emerson. 2003. Metabolic balance of the open sea. Nature **426:** 32.

Körtzinger, A., J. Schimanski, and U. Send. 2005. High quality oxygen measurements from profiling floats: A promising new technique. J. Atm. Ocean. Techn. **22:** 302–308.

———, ———, ———, and D. Wallace. 2004. The ocean takes a deep breath. Science **306:** 1337.

Laws, E. A., P. G. Falkowski, W. O. Smith Jr., H. Ducklow, and J. J. McCarthy. 2000. Temperature effects on export production in the upper ocean. Global Biogeochem. Cycles **14:** 1231–1246.

Lazarevich, P., T. Rossby, and C. McNeil. 2004. Oxygen variability in the near-surface waters of the northern North Atlantic: Observations and a model. J. Mar. Res. **62:** 663–683.

Li, Y.-H., and T.-H. Peng. 2002. Latitudinal change of remineralization ratios in the oceans and its implication for nutrient cycles. Global Biogeochem. Cycles **16:** 1130, doi:10.1029/2001GB001828.

Lima, I. D., and S. C. Doney. 2004. A three-dimensional, multinutrient, and size-structured ecosystem model for the North Atlantic. Global Biogeochem. Cycles **18:** GB3019, doi:10.1029/2003GB002146.

Martin, J. H., G. A. Knauer, D. M. Karl, and W. W. Broenkow. 1987. VERTEX: Carbon cycling in the northeast Pacific. Deep-Sea Res. **34:** 267–285.

Morel, A. 1988. Optical modeling of the upper ocean in relation to its biogenous matter content (case I waters). J. Geophys. Res. **93:** 10749–10768.

Musgrave, D. L., J. Chou, and W. J. Jenkins. 1988. Application of a model of upper-ocean physics for studying seasonal cycles of oxygen. J. Geophys. Res. **93:** 15679–15700.

NAJJAR, R. G., AND R. F. KEELING. 1997. Analysis of the mean annual cycle of the dissolved oxygen anomaly in the World Ocean. J. Mar. Res. **55:** 117–151.

PAULSON, C. A., AND J. J. SIMPSON. 1977. Irradiance measurements in the upper ocean. J. Phys. Oceanogr. **7:** 952–956.

PLATTNER, G.-K., N. GRUBER, H. FRENZEL, AND J. C. MCWILLIAMS. 2005. Decoupling marine export production from new production. Geophys. Res. Lett. **32:** L11612, doi:10.1029/2005GL022660.

PRICE, J. F., R. A. WELLER, AND R. PINKEL. 1986. Diel cycling: Observations and models of the upper ocean response to diurnal heating, cooling, and wind mixing. J. Geophys. Res. **91:** 8411–8427.

PRIMEAU, F. 2006. On the variability of the exponent in the power law depth dependence of POC flux estimated from sediment traps. Deep-Sea Res I **53:** 1335–1343.

RISER, S. C., AND K. S. JOHNSON. 2008. Net production of oxygen in the subtropical ocean. Nature **451:** 323–326.

SARMIENTO, J. L., AND N. GRUBER. 2006. Ocean biogeochemical dynamics. Princeton Univ. Press.

———, AND OTHERS. 2004. Response of ocean ecosystems to climate warming. Global Biogeochem. Cycles **18:** GB3003, doi:10.1029/2003GB002134.

SCHLITZER, R. 2002. Carbon export fluxes in the Southern Ocean: results from inverse modeling and comparison with satellite-based estimates. Deep-Sea Res. II **49:** 1623–1644.

———. 2007. Ocean Data View, http://odv.awi.de

SCHULENBERGER, E., AND J. L. REID. 1981. The Pacific shallow oxygen maximum, deep chlorophyll maximum, and primary productivity, reconsidered. Deep-Sea Res. Part A **28:** 901–919.

SIEGEL, D. A., S. C. DONEY, AND J. A. YODER. 2002. The North Atlantic spring phytoplankton bloom and Sverdrup's Critical Depth Hypothesis. Science **296:** 730–733.

SPITZER, W. S., AND W. J. JENKINS. 1989. Rates of mixing, gas exchange and new production: Estimates from seasonal cycles in the upper ocean near Bermuda. J. Mar. Res. **47:** 169–196.

STEINBERG, D. K., C. A. CARLSON, N. R. BATES, S. A. GOLDTHWAIT, L. P. MADIN, AND A. F. MICHAELS. 2000. Zooplankton vertical migration and the active transport of dissolved organic and inorganic carbon in the Sargasso Sea. Deep-Sea Res. I **47:** 137–158.

TENGBERG, A., AND OTHERS. 2006. Evaluation of a lifetime-based optode to measure oxygen in aquatic systems. Limnol. Oceanogr.: Methods **4:** 7–17.

TSUCHIYA, M., AND L. D. TALLEY. 1998. A Pacific hydrographic section at 88°W: Water-property distribution. J. Geophys. Res. **103:** 12899–12918.

YU, E.-F., AND OTHERS. 2001. Trapping efficiency of bottom-tethered sediment traps estimated from the intercepted fluxes of ^{230}Th and ^{231}Pa. Deep-Sea Res. I **48:** 865–889.

WANNINKHOF, R. 1992. Relationship between wind speed and gas exchange over the ocean. J. Geophys. Res. **97:** 7373–7382.

WOOLF, D. K., AND S. A. THORPE. 1991. Bubbles and the air-sea exchange of gasses in near-saturation conditions. J. Mar. Res. **49:** 435–466.

Received 29 August 2007
Accepted 24 March 2008
Amended 10 March 2008